



# Development of Lithium-Stuffed Garnet-Type Oxide Solid Electrolytes with High Ionic Conductivity for Application to All-Solid-State Batteries

Ryoji Inada\*, Satoshi Yasuda, Masaru Tojo, Keiji Tsuritani, Tomohiro Tojo and Yoji Sakurai

Department of Electrical and Electronic Engineering, Toyohashi University of Technology, Toyohashi, Japan

## OPEN ACCESS

### Edited by:

Jeff Sakamoto,  
University of Michigan, USA

### Reviewed by:

Hui Xia,  
Nanjing University of Science and  
Technology, China  
Candace K. Chan,  
Arizona State University, USA

### \*Correspondence:

Ryoji Inada  
inada@ee.tut.ac.jp

### Specialty section:

This article was submitted  
to Energy Storage,  
a section of the journal  
Frontiers in Energy Research

**Received:** 09 February 2016

**Accepted:** 06 July 2016

**Published:** 20 July 2016

### Citation:

Inada R, Yasuda S, Tojo M,  
Tsuritani K, Tojo T and Sakurai Y  
(2016) Development of Lithium-  
Stuffed Garnet-Type Oxide Solid  
Electrolytes with High Ionic  
Conductivity for Application to  
All-Solid-State Batteries.  
*Front. Energy Res.* 4:28.  
doi: 10.3389/fenrg.2016.00028

All-solid-state lithium-ion batteries are expected to be one of the next generations of energy storage devices because of their high energy density, high safety, and excellent cycle stability. Although oxide-based solid electrolyte (SE) materials have rather lower conductivity and poor deformability than sulfide-based ones, they have other advantages, such as their chemical stability and ease of handling. Among the various oxide-based SEs, lithium-stuffed garnet-type oxide, with the formula of  $\text{Li}_7\text{La}_3\text{Zr}_2\text{O}_{12}$  (LLZ), has been widely studied because of its high conductivity above  $10^{-4}$  S  $\text{cm}^{-1}$  at room temperature, excellent thermal performance, and stability against Li metal anode. Here, we present our recent progress for the development of garnet-type SEs with high conductivity by simultaneous substitution of  $\text{Ta}^{5+}$  into the  $\text{Zr}^{4+}$  site and  $\text{Ba}^{2+}$  into the  $\text{La}^{3+}$  site in LLZ.  $\text{Li}^+$  concentration was fixed to 6.5 per chemical formulae, so that the formula of our Li garnet-type oxide is expressed as  $\text{Li}_{6.5}\text{La}_{3-x}\text{Ba}_x\text{Zr}_{1.5-x}\text{Ta}_{0.5+x}\text{O}_{12}$  (LLBZT) and Ba contents  $x$  are changed from 0 to 0.3. As a result, all LLBZT samples have a cubic garnet structure without containing any secondary phases. The lattice parameters of LLBZT decrease with increasing  $\text{Ba}^{2+}$  contents  $x \leq 0.10$  while increase with  $x$  from 0.10 to 0.30, possibly due to the simultaneous change of  $\text{Ba}^{2+}$  and  $\text{Ta}^{5+}$  substitution levels. The relative densities of LLBZT are in a range between 89 and 93% and are not influenced in any significant way by the compositions. From the AC impedance spectroscopy measurements, the total (bulk + grain) conductivity at 27°C of LLBZT shows its maximum value of  $8.34 \times 10^{-4}$  S  $\text{cm}^{-1}$  at  $x = 0.10$ , which is slightly higher than the conductivity ( $= 7.94 \times 10^{-4}$  S  $\text{cm}^{-1}$ ) of LLZT without substituting Ba ( $x = 0$ ). The activation energy of the conductivity tends to become lower by Ba substitution, while excess Ba substitution degrades the conductivity in LLBZT. LLBZT has a wide electrochemical potential window of 0–6 V vs.  $\text{Li}^+/\text{Li}$ , and  $\text{Li}^+$  insertion and extraction reactions of  $\text{TiNb}_2\text{O}_7$  film electrode formed on LLBZT by aerosol deposition are demonstrated at 60°C. The results indicate that LLBZT can potentially be used as a SE in all-solid-state batteries.

**Keywords:** garnet-type oxide, solid electrolyte, ionic conductivity, all-solid-state battery, aerosol deposition

## INTRODUCTION

Lithium-ion batteries (LIBs) consist of a graphite negative electrode, organic liquid electrolyte, and lithium transition-metal oxide. They were first commercialized in 1991, and since then such batteries have been widely distributed globally as a power source for mobile electronic devices, such as cell phones and laptop computers. Nowadays, large-scale LIBs have been developed for application to automotive propulsion and stationary load-leveling for intermittent power generation from solar or wind energy (Tarascon and Armand, 2001; Armand and Tarascon, 2008; Scrosati and Garche, 2010; Goodenough and Kim, 2011). However, increasing battery size creates more serious safety issues for LIBs; one reason being the increased amount of flammable organic liquid electrolytes.

All-solid-state LIBs are expected to be one of the next generations of energy storage devices because of their high energy density, high safety, and excellent cycle stability (Fergus, 2010; Takada, 2013; Tatsumisago et al., 2013). The materials used for solid electrolyte (SE) must have not only high lithium-ion conductivity above  $10^{-3}$  S  $\text{cm}^{-1}$  at room temperature but also possess chemical stability against electrode materials, air, and moisture. Although oxide-based SE materials have rather lower conductivity and poor deformability compared to sulfide-based ones, they have other advantages such as their chemical stability and ease of handling (Knauth, 2009; Ren et al., 2015a). Furthermore, the formation of solid-solid interface with low resistance between SE and electrode is another challenging issue in order to achieve better electrochemical performance in solid-state batteries with an oxide-based SE.

Among the various oxide-based SE materials, lithium-stuffed garnet-type oxide with the formula of  $\text{Li}_7\text{La}_3\text{Zr}_2\text{O}_{12}$  (LLZ) has been widely studied because of its high conductivity above  $10^{-4}$  S  $\text{cm}^{-1}$  at room temperature, excellent thermal performance, and stability against Li metal anode (Murugan et al., 2007a). LLZ has two different crystal phases, one is the cubic phase (Awaka et al., 2011) and the other is tetragonal (Awaka et al., 2009a; Geiger et al., 2011), but high conductivity above  $10^{-4}$  S  $\text{cm}^{-1}$  at room temperature is mostly confirmed in cubic phase sintered at high temperature (1100–1200°C) in  $\text{Al}_2\text{O}_3$  crucible or with  $\text{Al}_2\text{O}_3$  substitution (Murugan et al., 2007a; Jin and McGinn, 2011; Kotobuki et al., 2011; Kumazaki et al., 2011; Li et al., 2012a; Rangasamy et al., 2012). During high temperature sintering,  $\text{Al}^{3+}$  enters from the crucible and/or substituted  $\text{Al}_2\text{O}_3$  into the LLZ pellet and works as sintering aid. In addition, it has been pointed out that some amount of  $\text{Al}^{3+}$  enters into the LLZ lattice, occupies the part of  $\text{Li}^+$  site and modifies the  $\text{Li}^+$  vacancy concentration for charge compensation, and stabilizes the cubic phase.  $\text{Ga}^{3+}$  has a similar effect as  $\text{Al}^{3+}$  for cubic phase stabilization and enhancement of ionic conducting properties (Wolfenstine et al., 2012; Shinawi and Janek, 2013; Bernuy-Lopez et al., 2014; Jalem et al., 2015).

Partial substitution of the  $\text{Zr}^{4+}$  site in LLZ by other higher valence cations, such as  $\text{Nb}^{5+}$  (Ohta et al., 2011; Kihira et al., 2013),  $\text{Ta}^{5+}$  (Buschmann et al., 2012; Li et al., 2012b; Logéat et al., 2012; Wang and Wei, 2012; Inada et al., 2014a; Thompson et al., 2014, 2015; Ren et al., 2015a,b),  $\text{W}^{6+}$  (Dhivya et al., 2013; Li et al., 2015), and  $\text{Mo}^{6+}$  (Bottke et al., 2015) is also reported to be effective in

stabilizing the cubic garnet phase, and their conductivity at room temperature is greatly enhanced up to  $\sim 1 \times 10^{-3}$  S  $\text{cm}^{-1}$  by controlling the contents of dopants and optimizing  $\text{Li}^+$  concentration in the garnet framework. Although a demonstration of a solid-state battery with Nb-doped LLZ as SE has been already reported (Ohta et al., 2012, 2013, 2014), it has also been reported that the chemical stability against a Li metal electrode of Ta-doped LLZ is much superior to a Nb-doped one (Nemori et al., 2015). Partially substituted  $\text{W}^{6+}$  in LLZ could potentially become a redox center as well as  $\text{Nb}^{5+}$  at relatively high potential against  $\text{Li}^+/\text{Li}$  (Xie et al., 2012).

In this paper, we synthesized garnet-type SEs with simultaneous substitution of  $\text{Ta}^{5+}$  into the  $\text{Zr}^{4+}$  site and  $\text{Ba}^{2+}$  into the  $\text{La}^{3+}$  site in LLZ, by a conventional solid state reaction method.  $\text{Li}^+$  concentration was fixed to 6.5 per chemical formulae to stabilize the cubic garnet phase, so that the chemical formula of our samples is expressed as  $\text{Li}_{6.5}\text{La}_{3-x}\text{Ba}_x\text{Zr}_{1.5-x}\text{Ta}_{0.5+x}\text{O}_{12}$  (LLBZT) and Ba contents  $x$  are changed from 0 to 0.30. Many researchers have pointed out that the  $\text{Li}^+$  conducting property in cubic garnet-type oxide is influenced not only by the  $\text{Li}^+$  concentration but also by the lattice constant (Thangadurai and Weppner, 2005; Murugan et al., 2007b; Awaka et al., 2009b; Kihira et al., 2013; Thangadurai et al., 2014, 2015). Since the ionic radii of  $\text{Ba}^{2+}$  (142 pm) is greater than  $\text{La}^{3+}$  (116 pm), the lattice sizes of LLBZT with fixed  $\text{Li}^+$  concentration per chemical formulae will be changed by the Ba substitution level, which will modify the ionic conducting property. Although it has been already confirmed that LLZ with substitution of both Ta and Ba can be fabricated (Tong et al., 2015), the influence of Ba substitution levels on the properties have not been fully discussed. In our study, the influence of Ba substitution level on the crystal phase, microstructure, and ionic conductivity for LLBZT was investigated. Furthermore, in order to investigate the feasibility for all-solid-state battery application, a  $\text{TiNb}_2\text{O}_7$  film electrode was formed on garnet-type LLBZT without any thermal treatment by an aerosol deposition (AD) method (Akedo, 2006) and its electrochemical properties were evaluated.

## MATERIALS AND METHODS

### Synthesis and Characterization of LLBZT

LLBZT oxides with fixed Li content of 6.5 but different Ba content  $x = 0, 0.05, 0.1, 0.20,$  and  $0.30$  were prepared by a conventional solid state reaction method. It should be noted that, in this work, we did not use an  $\text{Al}_2\text{O}_3$  crucible for sample synthesis because  $\text{Al}^{3+}$  contamination from the crucible into the LLBZT lattice during high temperature sintering may have an influence on  $\text{Li}^+$  concentration and that this contamination level is very difficult to control. In addition, we had already succeeded in obtaining cubic garnet-type Ta-doped LLZ without containing Al by using a Pt–Au alloy crucible and sintering at 1100°C for 15 h. The highest room temperature conductivity attains to  $6.1 \times 10^{-4}$  S  $\text{cm}^{-1}$  at  $\text{Li}^+$  concentration of 6.5 (Inada et al., 2014a), so we believe that  $\text{Al}^{3+}$  is not always required to stabilize the cubic phase and achieve high ionic conductivity.

Stoichiometric amounts of LiOH·H<sub>2</sub>O (Kojundo chemical laboratory, 99%, 10% excess was added to account for the evaporation of lithium at high temperatures), La(OH)<sub>3</sub> (Kojundo chemical laboratory, 99.99%), BaCO<sub>3</sub> (Kojundo chemical laboratory, 99.9%), ZrO<sub>2</sub> (Kojundo chemical laboratory, 98%), and Ta<sub>2</sub>O<sub>5</sub> (Kojundo chemical laboratory, 99.9%) were ground and mixed by planetary ball milling (Nagao System, Planet M2-3F) with zirconia balls and ethanol for 3 h and then calcined at 900°C for 6 h in a Pt–Au 5% alloy crucible. The calcined powders were ground again by planetary ball milling for 1 h, and then pressed into pellets at 300 MPa by cold isostatic pressing (CIP). Finally, all LLBZT pellets were sintered at 1150°C for 15 h in air using a Pt–Au 5% alloy crucible. During the sintering stage, the pellet was covered with the same mother powder to suppress excess Li loss and the formation of secondary phase, such as La<sub>2</sub>Zr<sub>2</sub>O<sub>7</sub>.

As the characterization of obtained LLBZT samples, the crystal structure of the samples was evaluated by X-ray diffraction (XRD, Rigaku Multiflex) using CuK $\alpha$  radiation ( $\lambda = 0.15418$  nm), with a measurement range of  $2\theta = 5\text{--}90^\circ$  and a step interval of  $0.004^\circ$ . Using the XRD data for all LLBZT samples, the lattice constants were calculated by Rigaku PDXL XRD analysis software. Scanning electron microscope (SEM) observation and energy dispersive X-ray (EDX) analysis were performed using a field-emission SEM (SU8000 Type II, Hitachi) to investigate the fractured surface microstructure of sintered LLBZT and the distribution of La, Ba, Zr, Ta, and O elements.

The conductivity of each LLBZT sample was evaluated with AC impedance measurements using a chemical impedance meter (3532-80, Hioki) and an LCR tester (3532-50, Hioki) at a temperature from 27 to 100°C, a frequency from 5 Hz to 5 MHz, and an applied voltage amplitude of 0.1 V. The former was used for measurement from 5 Hz to 1 MHz while the latter was used for measurement above 1 MHz, respectively. Both parallel surfaces of the pellet were sputtered with Li<sup>+</sup> blocking Au electrodes for the conductivity measurement. The electrochemical windows of the samples were evaluated by cyclic voltammetry (CV) using a potentiostat-galvanostat (VersaSTAT 3, Princeton Applied Research) at a scanning rate of  $0.2\text{ mV s}^{-1}$  between  $-0.4$  and  $6$  V vs. Li<sup>+</sup>/Li. An Au electrode and lithium metal were attached to both faces of the pellet as working and counter electrodes, respectively.

## TNO Film Electrode Fabrication on LLBZT and Its Characterization

In order to study the feasibility of LLBZT for application to solid state batteries, TiNb<sub>2</sub>O<sub>7</sub> (TNO) film electrode was formed on LLBZT pellet by AD method (Akedo, 2006). AD has several advantages compared to other conventional thin film deposition methods, including the deposition of a crystallized film without any heat treatments and a fast deposition rate. A film is deposited through impact and adhesion of fine particles on substrate at room temperature. This phenomenon is known as “room temperature impact consolidation (RTIC).” Consequently, as-deposited film has similar properties to the raw powder material, such as its crystal structure, composition, and physical property. By addressing these features, several papers have been reported for the feasibility of the AD method as a battery electrode or SE

fabrication process (Popovici et al., 2011; Kim et al., 2013; Inada et al., 2014b, 2015; Iwasaki et al., 2014; Ahn et al., 2015; Kato et al., 2016).

TNO is known to be an insertion-type electrode material operating at a potential around 1.6–1.7 V vs. Li<sup>+</sup>/Li and shows reversible charge and discharge capacities of around 250 mAh g<sup>-1</sup> and reasonably good cycle stability (Han et al., 2011; Guo et al., 2014; Ashisha et al., 2015), so that we considered TNO as suitable for the feasibility study for an all-solid-state battery application. TNO powders used in this work were prepared by a conventional solid-state reaction method. Stoichiometric amount of anatase TiO<sub>2</sub> (Kojundo Chemical Laboratory Co., Ltd., 99%) and Nb<sub>2</sub>O<sub>5</sub> (Kojundo Chemical Laboratory Co., Ltd., 99.9%) were ground and mixed in ethanol by planetary ball milling (Nagao System, Planet M2-3F) with zirconia balls for 1 h. The mixture was annealed at 1100°C for 24 h in air. From the XRD measurements, we confirmed that TNO was successfully obtained without forming any impurity phases.

It has been reported that both the size and morphology of raw powder are important factors for the structure and property of the film formed by AD (Akedo, 2006; Popovici et al., 2011; Inada et al., 2014b, 2015). In order to prepare TNO powder with suitable particle size for dense film fabrication by AD, TNO powder was pulverized using planetary ball milling (Nagao System, Planet M2-3F) with ethanol and zirconia balls. The rotation speed of planetary ball milling was fixed to 300 rpm but milling time was changed in order to control particle size.

The AD apparatus consists of a carrier gas supply system, an aerosol chamber, a deposition chamber equipped with a motored X–Y–Z stage, and a nozzle with a thin rectangular shaped-orifice with a size of 10 mm × 0.5 mm (Inada et al., 2014b, 2015). Deposition starts with evacuating the deposition chamber. A pressure difference between the carrier gas system and the deposition chamber is generated as a power source for film deposition. A carrier N<sub>2</sub> gas flows out from the gas supply system to the aerosol chamber. In the aerosol chamber, powder is dispersed into carrier gas and then the aerosol flows into the deposition chamber through a tube and is sprayed onto LLBZT as substrate. The deposition chamber was evacuated to a low vacuum state around 30 Pa, and deposition was carried out for several periods of 10 min. During the deposition process, the stage was moved uni-axially with a back-and-forth motion length of 50 mm. Distance between the tip of the nozzle and the LLBZT substrate was set to be 10 mm, and mass flow of N<sub>2</sub> carrier gas was fixed at 20 L min<sup>-1</sup>. Before depositing the film electrode, an end surface of the LLBZT pellet was polished using sandpaper in order to form a smooth interface with the electrolyte.

Scanning Electron Microscope observation was performed using a field-emission SEM (SU8000 Type II, Hitachi) to reveal the morphology of the TNO powder and both the surface and cross-sectional microstructure of the TNO film electrode formed on LLBZT. EDX analysis was also performed during SEM observation to investigate the distribution of Ti and Nb elements contained in the film electrode.

An all-solid-state cell was fabricated by attaching a Li metal foil on the opposite end surface of a LLBZT pellet covered by a TNO film electrode in an Ar-filled groove box. TNO film is

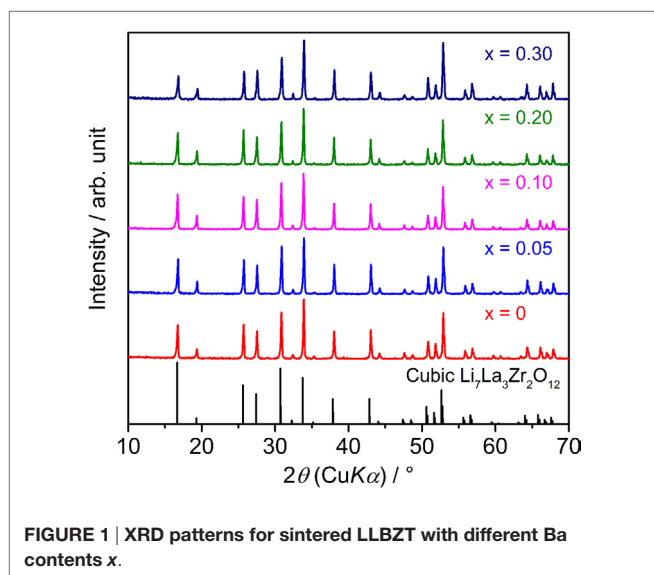
used as the working electrode and Li metal foil as the counter one. CV measurements (three cycles) of TNO film/LLBZT/Li all-solid-state cell were carried out using a potentiostat-galvanostat (VersaSTAT 3, Princeton Applied Research) at a temperature of 60°C and a scanning rate of 0.1 mV s<sup>-1</sup> between 1.0 and 2.5 V vs. Li<sup>+</sup>/Li. After the CV measurement, the solid-state cell was charged and discharged over a cell voltage range between 1.0 and 2.5 V at a constant current density of 2 μA cm<sup>-2</sup> (corresponding to 5 mA g<sup>-1</sup> per TNO film) and 60°C, using a battery test system (TOSCAT-3100, Toyo System).

## RESULTS AND DISCUSSION

### Characterization of LLBZT with Different Ba Contents

Figure 1 shows the XRD patterns of sintered LLBZT with different Ba content  $x = 0-0.30$ . Calculated diffraction peak patterns for cubic LLZ are also plotted as the reference (Awaka et al., 2011). All of the peaks for each LLBZT sample are well indexed as cubic garnet-type structures with a space group  $Ia\bar{3}d$ , and no other secondary phases were observed. Enlarged XRD patterns at  $2\theta = 50.0-54.5^\circ$  are shown in Figure 2. As can be seen, the peaks shifted toward a higher angle as  $x$  increases from 0 to 0.10, while at  $x \geq 0.10$ , the peaks shifted toward a lower angle with increasing  $x$ . It is worth noting that this trend is confirmed in other diffraction peaks, indicating that the lattice constants of LLBZT are not changed monotonically with  $x$ .

Using measured XRD data, we calculated the lattice constant for each LLBZT, and the results are summarized in Table 1. Among all the samples, LLBZT with  $x = 0.10$  has the smallest lattice constant (=12.944 Å). As confirmed in the chemical formulae of LLBZT prepared in this work, Ta contents  $y = 0.5 + x$  increase with Ba contents  $x$  and the ionic radii of Ta<sup>5+</sup> (64 pm) is smaller than Zr<sup>4+</sup> (78 pm). Therefore, the complex change of the lattice constants in LLBZT, depending on the composition, could be caused by the simultaneous change of Ba and Ta substitution



levels. At  $x \leq 0.10$ , increase of Ta<sup>5+</sup> substitution contents influences more on the lattice size of LLBZT, but at  $x > 0.10$ , the influence of Ba<sup>2+</sup> substitution contents on the lattice size become dominant. Consequently, the lattice constants of LLBZT are decreased with  $x \leq 0.10$ , while increased with  $x$  from 0.10 to 0.30.

The calculated lattice constants for all LLBZT are also plotted as a function of Ba contents  $x$  (lower horizontal axis) and Ta contents  $y = 0.5 + x$  (upper horizontal axis) in Figure 3. For comparison, the calculated lattice constants for Ba-free Li<sub>7-y</sub>La<sub>3</sub>Zr<sub>2-y</sub>Ta<sub>y</sub>O<sub>12</sub> (LLZT) with  $y = 0.50, 0.75$ , and 1.00 prepared in our previous work (Inada et al., 2014a) are also plotted against Ta contents  $y$ , which is almost linearly decreased with  $y$ . With increasing  $x$ , it is expected that the volume expansion of dodecahedral (La/Ba)O<sub>8</sub> and the volume contraction of octahedral (Ta/Zr)O<sub>6</sub> occur in a garnet framework of LLBZT, resulting in complex change of lattice constants depending on  $x$ . At Ba contents  $x \leq 0.10$  and Ta contents  $y \leq 0.60$ , the lattice constants for LLBZT nearly fall on the  $y$  dependence of lattice constants in LLZT, so that, for LLBZT with  $x \leq 0.10$  and  $y \leq 0.60$ , the contribution of a smaller Ta<sup>5+</sup> substitution to the Zr<sup>4+</sup> site is dominant. On the other hand, the lattice constants for LLBZT with  $x = 0.20$  and 0.30 and  $y = 1.70$  and 1.80 become larger than those for LLZT with the same  $y$  levels and the deviation becomes more remarkable with increasing  $x$ , suggesting that the contribution of a larger Ba<sup>2+</sup> substitution to the La<sup>3+</sup> site becomes dominant.

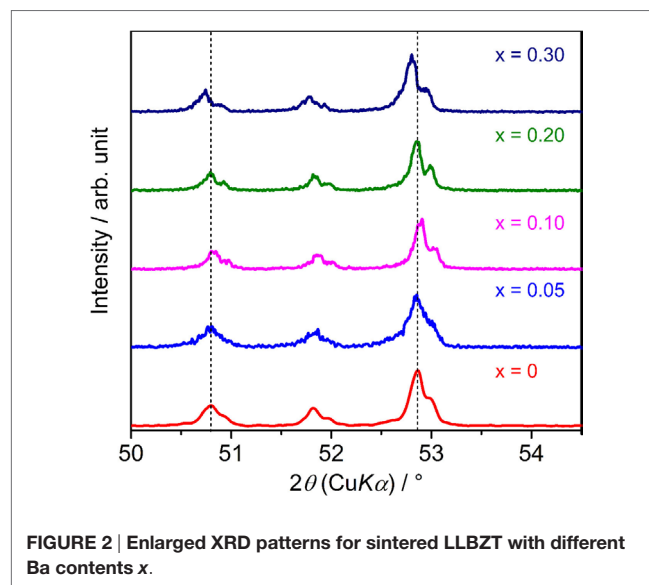


**TABLE 1 | Expected compositions, lattice constants, relative densities of sintered LLZT and LLBZT with different Ba contents  $x$ .**

Ba content $x$	Expected composition	Lattice constant/Å	Relative density %
0	Li <sub>6.5</sub> La <sub>3</sub> Zr <sub>1.5</sub> Ta <sub>0.5</sub> O <sub>12</sub>	12.954	92.8
0.05	Li <sub>6.5</sub> La <sub>2.95</sub> Ba <sub>0.05</sub> Zr <sub>1.45</sub> Ta <sub>0.55</sub> O <sub>12</sub>	12.949	92.6
0.10	Li <sub>6.5</sub> La <sub>2.9</sub> Ba <sub>0.1</sub> Zr <sub>1.4</sub> Ta <sub>0.6</sub> O <sub>12</sub>	12.944	90.4
0.20	Li <sub>6.5</sub> La <sub>2.8</sub> Ba <sub>0.2</sub> Zr <sub>1.3</sub> Ta <sub>0.7</sub> O <sub>12</sub>	12.952	88.8
0.30	Li <sub>6.5</sub> La <sub>2.7</sub> Ba <sub>0.3</sub> Zr <sub>1.2</sub> Ta <sub>0.8</sub> O <sub>12</sub>	12.964	92.0

**Figure 4** shows the comparison of SEM images for fractured cross sections of all LLBZT. Average grain size in the sintered LLBZT samples was confirmed to be around 5  $\mu\text{m}$ , and all grains are in good contact with each other. The density of each sintered pellet was determined from their weight and physical dimensions. The relative density (measured density normalized by the theoretical one) of LLBZT with different compositions are summarized in **Table 1**. Here, the theoretical density for each sample was calculated from the lattice constant and expected compositions also shown in **Table 1**. The relative density of each sample was estimated to be in a range between 89 and 93%, indicating

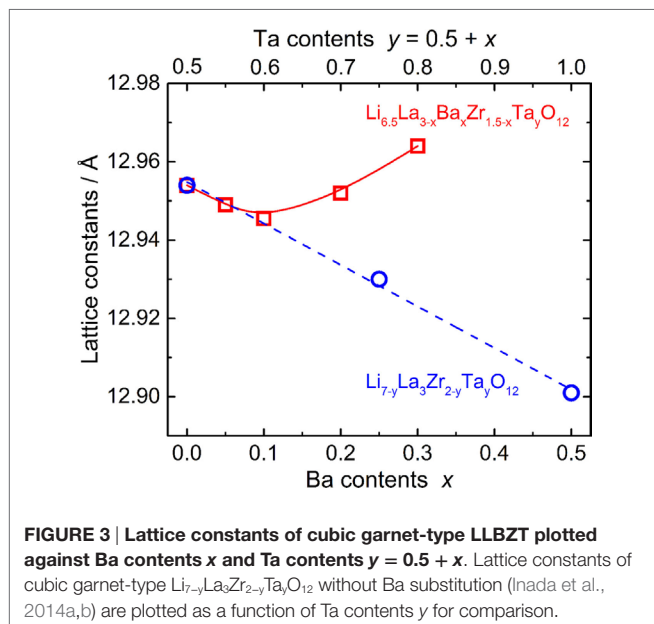


**FIGURE 3 |** Lattice constants of cubic garnet-type LLBZT plotted against Ba contents  $x$  and Ta contents  $y = 0.5 + x$ . Lattice constants of cubic garnet-type  $\text{Li}_{7-y}\text{La}_3\text{Zr}_{2-y}\text{Ta}_y\text{O}_{12}$  without Ba substitution (Inada et al., 2014a,b) are plotted as a function of Ta contents  $y$  for comparison.

that the difference in relative density among the sintered LLBZT with different composition is not so large. Enlarged SEM images and corresponding elementary mapping for La, Ba, Zr, and Ta and O in LLBZT with different Ba contents  $x = 0.05$ – $0.30$  are also shown in **Figure 5**. It can be seen that all elements show similar distribution in the sample, indicating that  $\text{La}^{3+}$  and  $\text{Zr}^{4+}$  are successfully substituted by  $\text{Ba}^{2+}$  and  $\text{Ta}^{5+}$ , respectively.

## Ionic Conductivity and Electrochemical Stability of LLBZT

The conductivity of LLBZT with different compositions was examined by AC impedance spectroscopy using a Li-ion-blocking Au electrode. **Figure 6** shows Nyquist plots of AC impedance measured at 27 and 50°C for all samples. For direct comparison among the samples with different sizes, real and imaginary parts of impedance  $Z$  and  $Z''$  multiplied by a factor of  $AL^{-1}$  are plotted, where  $A$  and  $L$  are surface area and thickness of each pellet. For all samples, a part of the semicircle and linear portion data were obtained in high and low frequency regions, indicating that the conducting nature is primarily ionic. Only a part of one semicircle was confirmed and the intercept point of the linear tail in the low frequency range with a real axis corresponding to the sum of the bulk- and grain-boundary resistance. Total conductivity  $\sigma$  for each sample can be calculated by the inverse of the total (bulk and grain boundary) resistance.

The lattice constant and conductivity  $\sigma$  at 27°C of LLBZT are plotted against Ba contents  $x$  in **Figures 7A,B**. The sample without Ba substitution shows  $\sigma = 7.94 \times 10^{-4} \text{ S cm}^{-1}$ , which is higher than LLZT with the same composition reported in our previous work (Inada et al., 2014a). This is mainly due to the higher sintering temperature ( $=1150^\circ\text{C}$ ) used in this work than that used in previous work ( $=1100^\circ\text{C}$ ). At  $x \leq 0.1$ ,  $\sigma$  of LLBZT slightly increases, while the lattice constants slightly decrease with

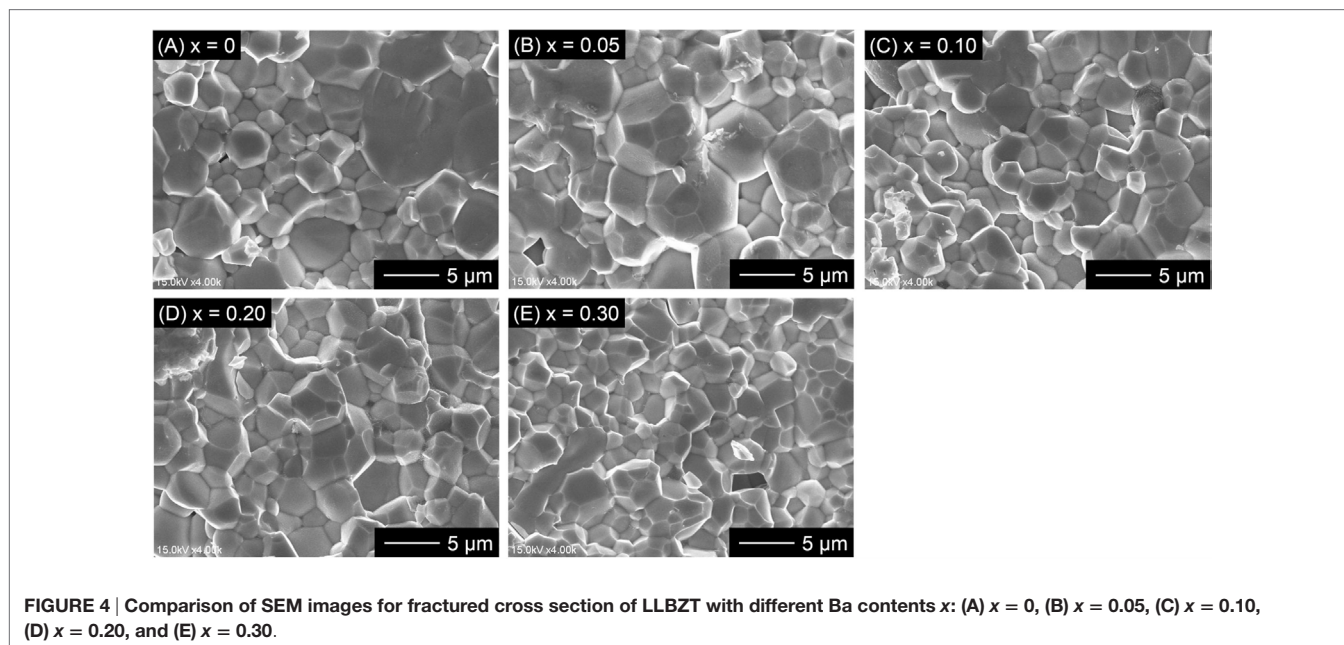


**FIGURE 4 |** Comparison of SEM images for fractured cross section of LLBZT with different Ba contents  $x$ : (A)  $x = 0$ , (B)  $x = 0.05$ , (C)  $x = 0.10$ , (D)  $x = 0.20$ , and (E)  $x = 0.30$ .

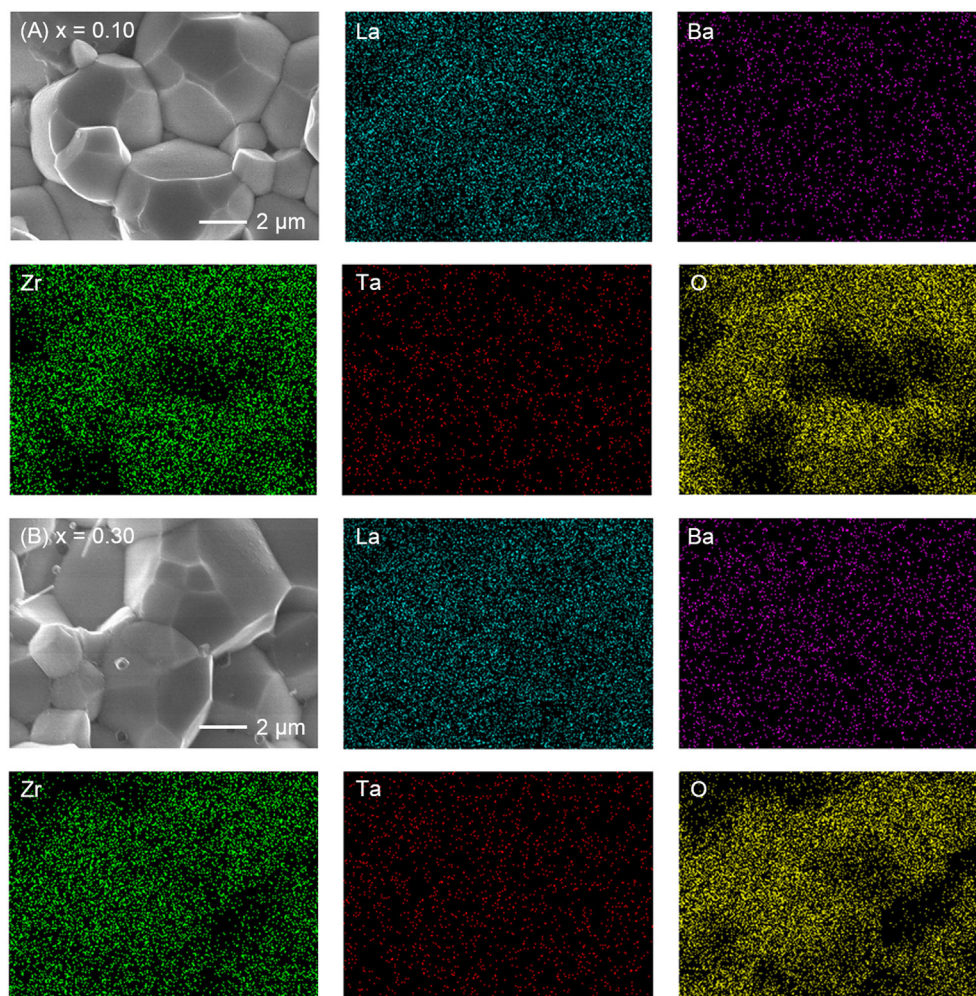


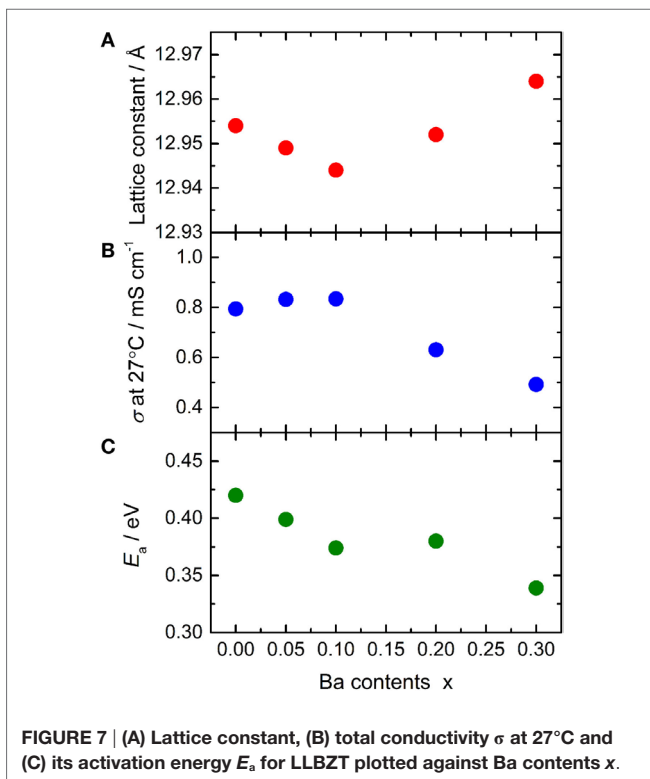
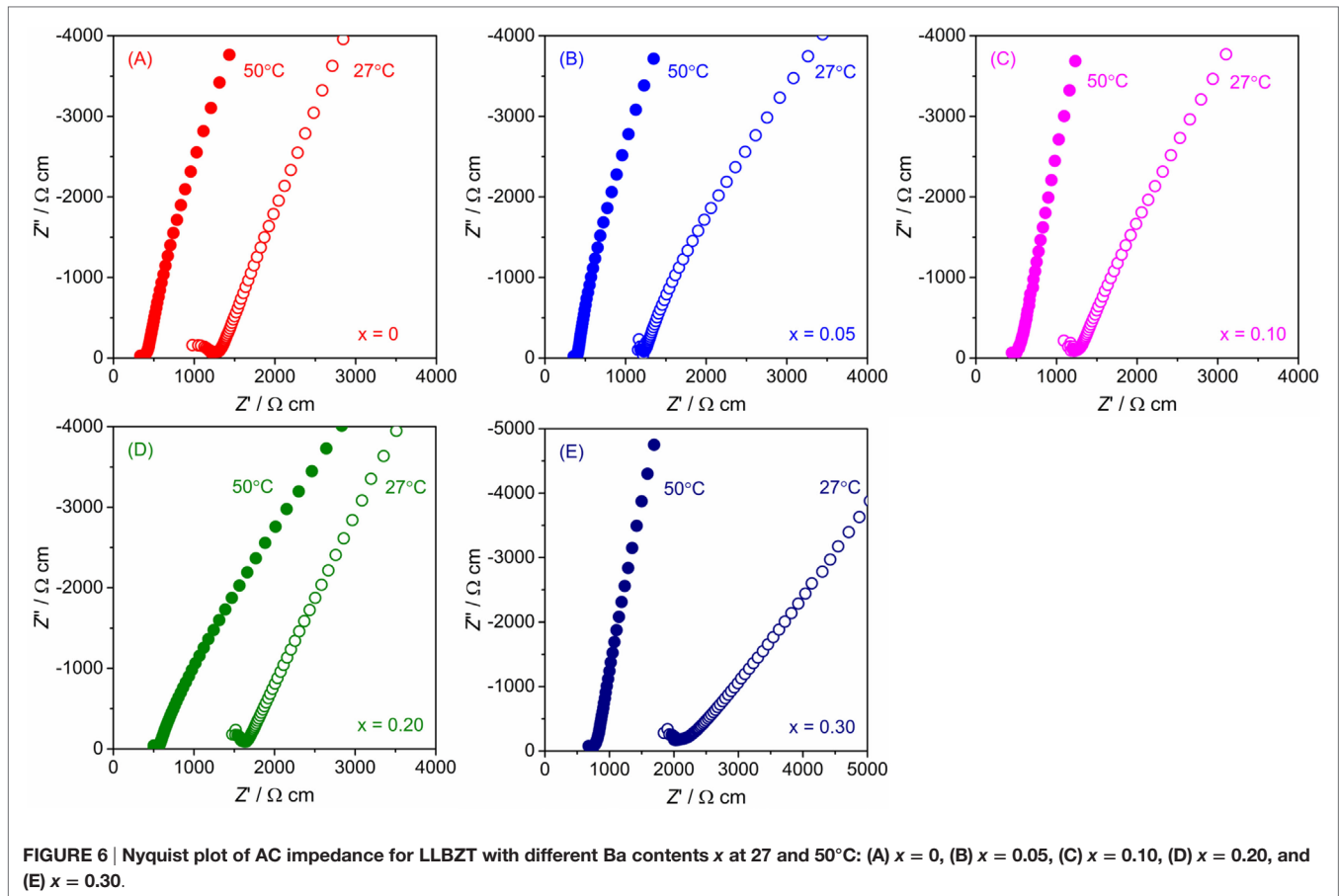
**FIGURE 5 |** SEM images and corresponding elementary mapping for La, Ba, Zr, Ta, and O for LLBZT with (A)  $x = 0.10$  and (B)  $x = 0.30$ .

increasing  $x$ . The highest  $\sigma = 8.34 \times 10^{-4} \text{ S cm}^{-1}$  was obtained in LLBZT with  $x = 0.1$  and the smallest lattice constant ( $=12.944 \text{ \AA}$ ) among all samples. The relative density of LLBZT with  $x = 0.1$  is slightly smaller than that for the sample with  $x = 0$  and  $0.05$ . Unfortunately, we could not obtain the bulk ionic conductivity of LLBZT, quantitatively, because of the limitation of frequency ranges in our experimental set-up, but it is expected that the bulk conductivity of LLBZT shows its maximum at  $x = 0.1$ . At  $x > 0.1$ ,  $\sigma$  monotonically decreases while the lattice constants increase with  $x$ . The lowest  $\sigma = 4.92 \times 10^{-4} \text{ S cm}^{-1}$  was confirmed in LLBZT with  $x = 0.3$  and the largest lattice constant among all samples.

The conductivity of LLBZT with fixed  $\text{Li}^+$  concentration ( $=6.5$ ) shows its maximum at a lattice constant of around  $12.94\text{--}12.95 \text{ \AA}$ . Kihira et al. (2013) have reported their systematical investigation for the properties of cubic garnet-type LLZ with substituting  $\text{Nb}^{5+}$  to  $\text{Zr}^{4+}$  site and alkali earth metal cations, such as  $\text{Sr}^{2+}$  and  $\text{Ca}^{2+}$ , to  $\text{La}^{3+}$  site simultaneously, to modify the lattice constant. They also tried to substitute  $\text{Mg}^{2+}$  and  $\text{Ba}^{2+}$  to  $\text{La}^{3+}$  site in Nb-doped LLZ but some impurity phases, such as  $\text{MgO}$  and  $\text{BaZrO}_3$ , were formed.

Interestingly, regardless of the substitution element, the highest conductivity in their samples is observed at nearly the same lattice constant of  $12.94\text{--}12.96 \text{ \AA}$ , which is close to our results for LLBZT with  $x = 0\text{--}0.10$ . However, LLBZT with  $x = 0.20$  has lower room temperature conductivity than LLBZT with  $x = 0.05$ , although both samples have nearly the same lattice size.

Since the difference in the relative densities among all samples is not so large, the contribution of grain-boundary resistivity to the total ionic conductivity does not depend on the composition of LLBZT. We believe that the composition dependence of  $\sigma$  is mainly caused by the change of  $\text{Li}^+$  conduction property in LLBZT bulk. The bulk  $\text{Li}^+$  conductivity  $\sigma_{\text{Li}}$  is described as  $\sigma_{\text{Li}} = ne\mu$ , where  $n$  is the number of carriers,  $e$  is the charge and  $\mu$  is the carrier mobility. Since the charge value will be constant,  $\sigma_{\text{Li}}$  will be influenced by the number of carriers and the mobility. As mentioned above, it is expected that in LLBZT garnet, the volume of the dodecahedral  $(\text{La/Ba})\text{O}_8$  is expanded while the volume of octahedral  $(\text{Ta/Zr})\text{O}_6$  is contracted with increasing Ba contents  $x$ . These polyhedrons are adjacent to the tetrahedral  $\text{LiO}_4$  and the



octahedral  $\text{LiO}_6$  in a garnet framework, so that the volumes of the  $\text{LiO}_4$  and  $\text{LiO}_6$  polyhedrons also show complex change depending on  $x$ . It has been pointed out that the  $\text{Li}^+$  conductivity of garnet-type oxides is strongly influenced by the site occupancy in both  $\text{LiO}_4$  (24d site) and  $\text{LiO}_6$  (96h site) polyhedrons. The 24d and 96h site occupancies effect on the number of carriers, and higher  $\sigma_{\text{Li}}$  is achieved by well-balanced site occupancy (Li et al., 2012b; Kihira et al., 2013; Thangadurai et al., 2014, 2015). We believe that the 24d and 96h site occupancies are influenced not only by the  $\text{Li}^+$  contents in a garnet framework but also by the sizes of both  $\text{LiO}_4$  and  $\text{LiO}_6$  polyhedrons. The highest conductivity at room temperature for LLBZT with  $x$  from 0.05 to 0.10 would be attributed to the well-balanced 24d and 96h site occupancies, while the deterioration of the conductivity with increasing  $x > 0.20$  would be caused by the change in the site occupancies depending on the sizes of both  $\text{LiO}_4$  and  $\text{LiO}_6$  polyhedrons.

Temperature dependence of the conductivity for all LLBZT was also evaluated in the temperature range from 27 to 100°C. **Figure 8** shows the variation of  $\sigma$  for all sintered samples as a function of an inverse of temperature  $1000T^{-1}$ . The temperature dependence of  $\sigma$  is expressed by the Arrhenius equation as  $\sigma = \sigma_0 \exp[-E_a/(k_B T)]$ , where  $\sigma_0$  is constant,  $E_a$  is activation energy of conductivity, and  $k_B$  is Boltzmann constant ( $= 1.381 \times 10^{-23}$  J/K). The  $E_a$  of each sample are estimated from the slope of  $\sigma T$  data plotted in **Figure 8** and summarized in **Table 2**, together with  $\sigma$  at 27°C. The sample without Ba

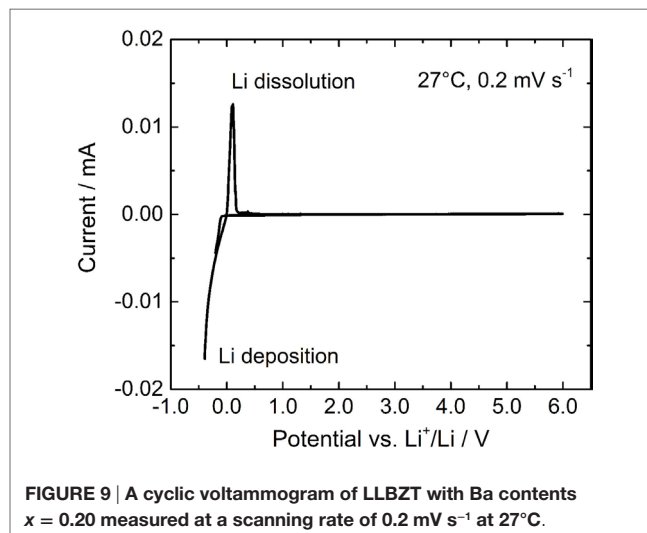
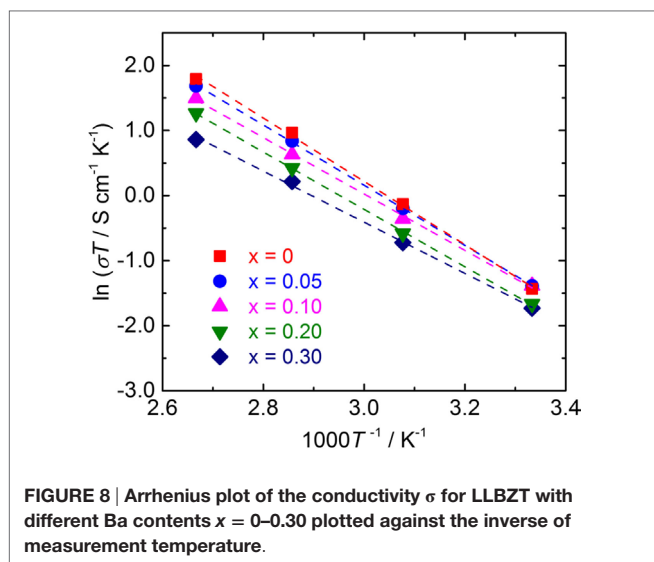


**TABLE 2 |** Total conductivity  $\sigma$  at different measurement temperature and activation energy  $E_a$  for LLBZT with different Ba contents  $x = 0-0.30$ .

Ba content $x$	Total conductivity $\sigma/\text{S cm}^{-1}$				$E_a/\text{eV}$
	27°C	50°C	75°C	100°C	
0	$7.94 \times 10^{-4}$	$2.70 \times 10^{-3}$	$7.5 \times 10^{-3}$	$16.0 \times 10^{-3}$	0.420
0.05	$8.32 \times 10^{-4}$	$2.50 \times 10^{-3}$	$6.6 \times 10^{-3}$	$14.4 \times 10^{-3}$	0.399
0.10	$8.34 \times 10^{-4}$	$2.20 \times 10^{-3}$	$5.40 \times 10^{-3}$	$11.9 \times 10^{-3}$	0.374
0.20	$6.31 \times 10^{-4}$	$1.80 \times 10^{-3}$	$4.50 \times 10^{-3}$	$10.6 \times 10^{-3}$	0.380
0.30	$4.92 \times 10^{-4}$	$1.30 \times 10^{-3}$	$3.10 \times 10^{-3}$	$5.40 \times 10^{-3}$	0.339

substitution has the highest  $E_a = 0.42 \text{ eV}$ , which is higher than an Al-doped LLZT sample with a similar composition (Li et al., 2012b) but nearly the same as the Al-free sample prepared by hot pressing (Thompson et al., 2015). The  $E_a$  of LLBZT is in the range of 0.34–0.40 eV and tends to decrease with increasing Ba substitution levels as shown in **Figure 7C**.

Ba substitution levels influence on both the ionic conductivity and its activation energy. At  $x \leq 0.10$ , the lattice size of LLBZT is reduced with increasing  $x$ , while  $\sigma$  at room temperature is increased slightly, suggesting that the number of carriers for  $\text{Li}^+$  conduction in LLBZT are increased with  $x$  from 0 to 0.10. Therefore, the reduction of  $E_a$  by Ba substitution at  $x \leq 0.10$  would be mainly attributed to the increase in the number of carriers by the slight modification of the  $24d$  and  $96h$  site occupancies. On the other hand, the lattice size of LLBZT is increased with  $x$ , while  $\sigma$  at room temperature is lowered with increasing  $x$  from 0.10 to 0.30, suggesting that the number of carriers for  $\text{Li}^+$  conduction is decreased with  $x$  while the bottleneck size for  $\text{Li}^+$  conduction expands. It is expected that the expansion of bottleneck size result in enhancing the mobility, so the reduction of  $E_a$  at  $x > 0.10$  would be mainly caused by the enhancement of the mobility.

In order to evaluate the electrochemical stability of LLBZT, a cyclic voltammogram of LLBZT is shown in **Figure 9**. Li deposition and dissolution peaks near 0 V vs.  $\text{Li}^+/\text{Li}$  are clearly observed, but no other reactions are confirmed up to 6 V vs.  $\text{Li}^+/\text{Li}$ . Therefore, LLBZT has a wide electrochemical potential

window and various electrode materials can potentially be used to construct all-solid-state batteries with LLBZT as the SE.

## Characterization of TNO Film Electrode Formed on LLBZT

For the feasibility study of all-solid-state battery application, TNO film electrode was formed on the surface of sintered LLBZT pellet by the AD method, and its electrochemical property was evaluated. We used pulverized TNO powder by planetary ball milling as raw material for fabrication of the film electrode. As can be seen in **Figure 10A**, raw TNO powder dominantly includes particles with a size of 0.5–0.8  $\mu\text{m}$ . SEM images of the surface and cross section of TNO film electrode are shown in **Figures 10B,C**, together with a schematic illustration of the film formation by AD in **Figure 10D**. It is confirmed that strongly deformed and/or fractured TNO particles form a dense film electrode on LLBZT without any thermal treatment. The thickness of the TNO film electrode is confirmed to be  $\sim 1.5 \mu\text{m}$ . The interface morphology between the TNO film and the LLBZT pellet seems to be very smooth. **Figure 11** shows elementary mapping results of Ti and Nb on the surface and the cross section of the TNO film electrode formed on LLBZT. On the film surface, both Ti and Nb are detected in the whole observed area, while in the cross section, Ti and Nb are dominantly detected in the film electrode area.

A cyclic voltammogram of a TNO film/LLBZT/Li solid-state cell measured at  $60^\circ\text{C}$  and a scan rate of  $0.1 \text{ mV s}^{-1}$  is shown in **Figure 12**. After the cell construction, the open-circuit voltage of the cell was confirmed to be around 1.7 V. Except for the first scanning toward anodic direction, both the oxidation and reduction reaction of the TNO film electrode on LLBZT seems to be reversible. Broad oxidation and reduction reaction peaks are confirmed at the cell voltages (nearly corresponding to the potential vs.  $\text{Li}^+/\text{Li}$ ) of 1.8 V and 1.6 V, which corresponds to the  $\text{Li}^+$  extraction and insertion reaction potential for TNO (Ashisha et al., 2015). **Figure 13** shows the charge and discharge properties of a TNO film/LLBZT/Li solid-state cell measured at

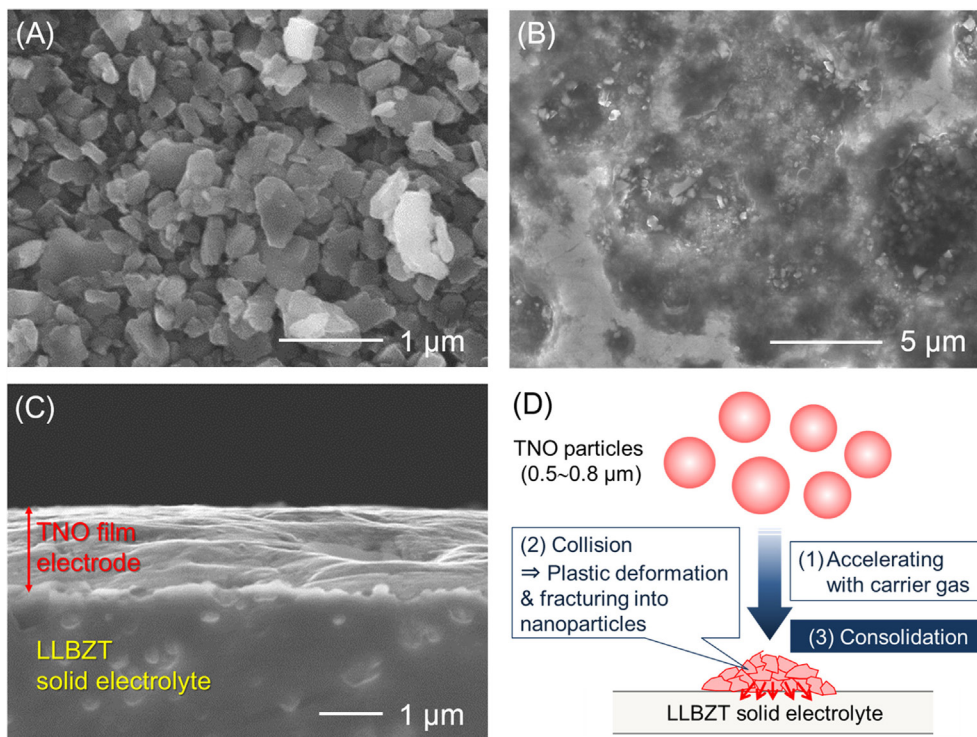


**FIGURE 10 |** SEM images for (A) TNO powder used as raw materials for film electrode fabrication by AD, (B) the surface of TNO film electrode, and (C) polished cross section of TNO film electrode. Plastically deformed and/or fractured TNO particles form the dense film on LLBZT via impact consolidation as shown in (D).

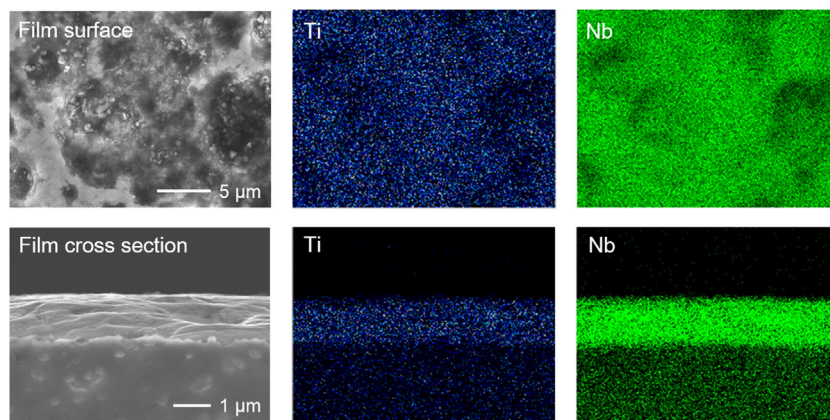
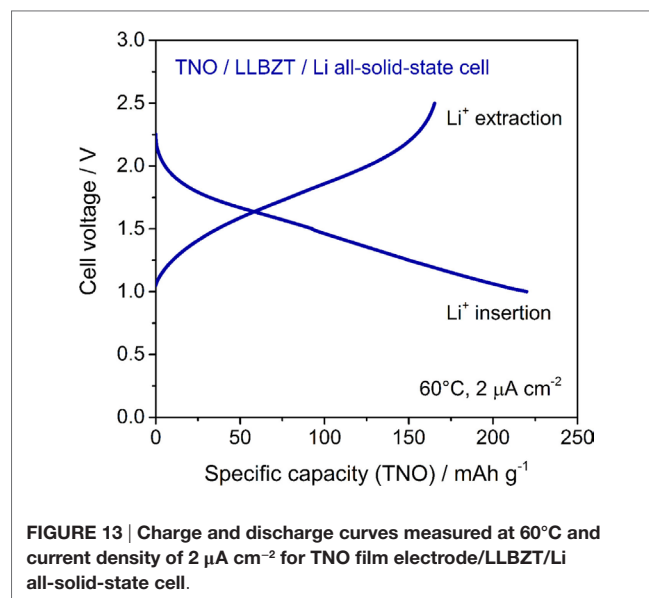
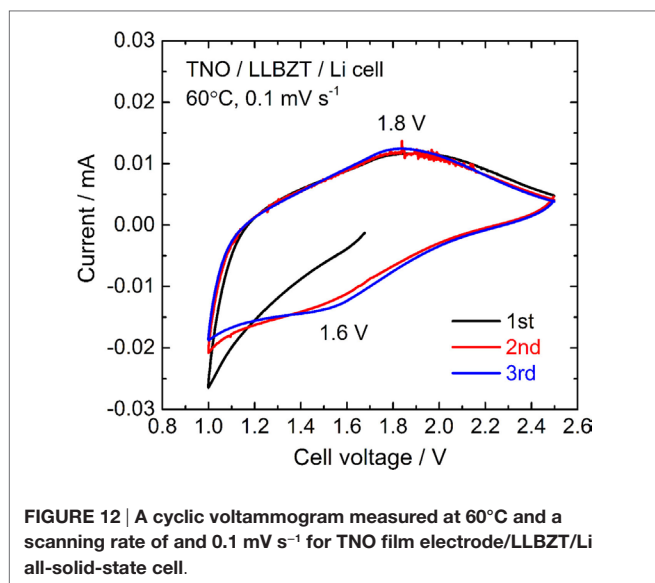


**FIGURE 11 |** SEM images and corresponding elementary mapping for Ti and Nb on the surface and polished cross section of TNO film electrode formed on LLBZT.

60°C and a current density of  $2 \mu\text{A cm}^{-2}$ . As can be seen, TNO film electrode formed on LLBZT by AD showed capacities of  $220 \text{ mAh g}^{-1}$  for  $\text{Li}^+$  insertion reaction and  $170 \text{ mAh g}^{-1}$  for  $\text{Li}^+$  extraction reaction. Electrode reactions occur at an averaged cell voltage of 1.6 V, which is nearly the same as the TNO composite electrode with conducting additive and binder in an organic

liquid electrolyte (Han et al., 2011; Guo et al., 2014; Ashisha et al., 2015). Although the coulombic efficiency of TNO film electrode is far below 100% at present, the results shown in **Figures 12** and **13** indicate that LLBZT works as the  $\text{Li}^+$  conduction path between the TNO film as the working electrode and the Li metal foil as the counter one.



As a future prospect for solid state battery development with garnet-type LLBZT SE, both increasing the thickness of the electrode and reducing the thickness of the SE layer should be indispensable for enhancing the volumetric energy density of a solid-state battery. In a thicker electrode layer with a thickness of several 10 μm, a composite structure with electrode active material and SE must be needed to increase the solid–solid interface among them for the high utilization of active material in a composite electrode. We are considering that AD is one of the potential processing methods to form composite electrode on LLBZT sheet because composite powders with active material and Li<sup>+</sup> conducting SE can be directly used (Iwasaki et al., 2014; Kato et al., 2016) as raw material to form the composite electrode on SE sheet. Since thermal treatment is not always needed to form the electrode on SE sheet by AD, undesired reactions between the electrode and SE can be greatly suppressed. In addition, AD is also potentially applicable to the fabrication of film-shaped SE layer, which has been already demonstrated in NASICON-type Li<sup>+</sup> conducting oxide-based SE (Popovici et al., 2011; Inada et al., 2015). We are now trying to fabricate composite thick film electrode on LLBZT by AD, and progress on this will be reported in a forthcoming paper.

## CONCLUSION

In this paper, we investigate the properties of garnet-type Li<sup>+</sup> conducting oxide SEs with simultaneous substitution of Ta<sup>5+</sup> into the Zr<sup>4+</sup> site and Ba<sup>2+</sup> into the La<sup>3+</sup> site in LLZ. Li<sup>+</sup> concentration was fixed to 6.5 per chemical formulae, so that the composition of our samples is expressed as Li<sub>6.5</sub>La<sub>3-x</sub>Ba<sub>x</sub>Zr<sub>1.5-x</sub>Ta<sub>0.5+x</sub>O<sub>12</sub> (LLBZT), and Ba contents  $x$  are changed from 0 to 0.30. As a result, all LLBZT samples have a cubic garnet-type structure without any secondary phases. The lattice constants of LLBZT decrease with increasing Ba<sup>2+</sup> contents  $x \leq 0.10$  while increase with  $x$  from 0.10 to 0.30, possibly caused by the simultaneous change of smaller

Ta<sup>5+</sup> and larger Ba<sup>2+</sup> substitution levels. On the other hand, the relative densities of LLBZT are not influenced greatly by  $x$ . The total conductivity at 27°C of LLBZT has its maximum value of  $8.34 \times 10^{-4}$  S cm<sup>-1</sup> at  $x = 0.10$ , which is slightly higher than the conductivity of LLZT without substituting Ba ( $= 7.94 \times 10^{-4}$  S cm<sup>-1</sup>). This improvement would be attributed to the modification of the number of carriers by tuning the 24d and 96h site occupancies. A larger lattice size created by excess Ba substitution is not suitable to achieve high ionic conductivity in LLBZT. The activation energy of the conductivity tends to become lower than the sample without Ba substitution. However, the influence of Ba contents on the Li<sup>+</sup> occupation site and carrier concentration in garnet-type LLBZT cannot be examined at present so that a detailed structural analysis would be necessary to clarify the ionic conducting property in LLBZT.

LLBZT is confirmed to be electrochemically stable at the potential range of 0–6 V vs. Li<sup>+</sup>/Li so that various kinds of electrode materials can potentially be used for constructing an all-solid-state battery. In order to investigate the feasibility for solid-state battery application, TNO film electrode was formed on LLBZT without any thermal treatment by an AD method, and its electrochemical properties were evaluated. The Li<sup>+</sup> insertion and extraction reaction of the film electrode formed on LLBZT could be confirmed, indicating that LLBZT can be used as a SE in an all-solid-state battery.

## AUTHOR CONTRIBUTIONS

RI was in charge of planning and performing all the experiment (containing both material preparation and characterization) in this work, together with summarizing the paper preparation. SY and KT were in charge of the preparation and characterization of oxide solid electrolyte samples. MT was in charge of the fabrication of the film-type electrode on solid electrolyte material and its characterization. TT and YS were in charge of the discussion for all experimental results.

## ACKNOWLEDGMENTS

RI would like to thank Prof. Dr. Venkataraman Thangadurai of University of Calgary, Prof. Dr. Jeff Sakamoto of University of Michigan, Prof. Dr. Palani Balaya of National University of Singapore, and Prof. Dr. Ashutosh Tiwari of The University of Utah for their kind and technical advices in our sample preparation

## REFERENCES

Ahn, C.-W., Choi, J.-J., Ryu, J., Hahn, B.-D., Kim, J.-W., Yoon, W.-Ha, et al. (2015). Microstructure and electrochemical properties of iron oxide film fabricated by aerosol deposition method for lithium ion battery. *J. Power Sources* 275, 336–340. doi:10.1016/j.jpowsour.2014.11.033

Akedo, J. (2006). Aerosol deposition of ceramic thick films at room temperature: densification mechanism of ceramic layers. *J. Am. Ceramic Soc.* 89, 1834–1839. doi:10.1111/j.1551-2916.2006.01030.x

Armand, M., and Tarascon, J.-M. (2008). Building better batteries. *Nature* 451, 652–657. doi:10.1038/451652a

Ashisha, A. G., Arunkumara, P., Babua, B., Manikandana, P., Saranga, S., and Shaijumon, M. M. (2015). TiNb<sub>2</sub>O<sub>7</sub>/graphene hybrid material as high performance anode for lithium-ion batteries. *Electrochim. Acta* 176, 285–292. doi:10.1016/j.electacta.2015.06.122

Awaka, J., Kijima, N., Hayakawa, H., and Akimoto, J. (2009a). Synthesis and structure analysis of tetragonal Li<sub>7</sub>La<sub>3</sub>Zr<sub>2</sub>O<sub>12</sub> with the garnet-related type structure. *J. Solid State Chem.* 182, 2046–2052. doi:10.1016/j.jssc.2009.05.020

Awaka, J., Kijima, N., Takahashi, Y., Hayakawa, H., and Akimoto, J. (2009b). Synthesis and crystallographic studies of garnet-related lithium-ion conductors Li<sub>6</sub>CaLa<sub>2</sub>Ta<sub>2</sub>O<sub>12</sub> and Li<sub>6</sub>BaLa<sub>2</sub>Ta<sub>2</sub>O<sub>12</sub>. *Solid State Ionics*. 180, 602–606. doi:10.1016/j.ssi.2008.10.022

Awaka, J., Takashima, A., Kataoka, K., Kijima, N., Idemoto, Y., and Akimoto, J. (2011). Crystal structure of fast lithium-ion-conducting cubic Li<sub>7</sub>La<sub>3</sub>Zr<sub>2</sub>O<sub>12</sub>. *Chem. Lett.* 40, 60–62. doi:10.1246/cl.2011.60

Bernuy-Lopez, C., Manalastas, W. Jr., Lopez, J. M., Aguadero, A., Aguesse, F., and Kilner, J. A. (2014). Atmosphere controlled processing of Ga-substituted garnets for high Li-ion conductivity ceramics. *Chem. Mater.* 26, 3610–3617. doi:10.1021/cm5008069

Bottke, P., Rettenwander, D., Schmidt, W., Amthauer, G., and Wilkening, M. (2015). Ion dynamics in solid electrolytes: NMR reveals the elementary steps of Li<sup>+</sup> hopping in the garnet Li<sub>6.5</sub>La<sub>3</sub>Zr<sub>1.75</sub>Mo<sub>0.25</sub>O<sub>12</sub>. *Chem. Mater.* 27, 6571–6582. doi:10.1021/acs.chemmater.5b02231

Buschmann, H., Berendts, S., Mogwitz, B., and Janek, J. (2012). Lithium metal electrode kinetics and ionic conductivity of the solid lithium ion conductors “Li<sub>7</sub>La<sub>3</sub>Zr<sub>2</sub>O<sub>12</sub>” and Li<sub>7-x</sub>La<sub>3</sub>Zr<sub>2-x</sub>Ta<sub>x</sub>O<sub>12</sub> with garnet-type structure. *J. Power Sources* 206, 236–244. doi:10.1016/j.jpowsour.2012.01.094

Dhivya, L., Janani, N., Palanivel, B., and Murugan, R. (2013). Li<sup>+</sup> transport properties of W substituted Li<sub>7</sub>La<sub>3</sub>Zr<sub>2</sub>O<sub>12</sub> cubic lithium garnets. *AIP Adv.* 3, 082115. doi:10.1063/1.4818971

Fergus, J. W. (2010). Ceramic and polymeric solid electrolytes for lithium-ion batteries. *J. Power Sources* 195, 4554–4569. doi:10.1016/j.jpowsour.2010.01.076

Geiger, C. A., Alekseev, E., Lazic, B., Fisch, M., Armbruster, T., Langner, R., et al. (2011). Crystal chemistry and stability of “Li<sub>7</sub>La<sub>3</sub>Zr<sub>2</sub>O<sub>12</sub>” garnet: a fast lithium-ion conductor. *Inorg. Chem.* 50, 1089–1097. doi:10.1021/ic101914e

Goodenough, J. B., and Kim, Y. (2011). Challenges for rechargeable batteries. *J. Power Sources* 196, 6688–6694. doi:10.1016/j.jpowsour.2010.11.074

Guo, B. K., Yu, X. Q., Sun, X. G., Chi, M. F., Qiao, Z. A., Liu, J., et al. (2014). A long-life lithium-ion battery with a highly porous TiNb<sub>2</sub>O<sub>7</sub> anode for large-scale electrical energy storage. *Energy Environ. Sci.* 7, 2220–2226. doi:10.1039/C4EE00508B

Han, J.-T., Huan, Y.-H., and Goodenough, J. B. (2011). New anode framework for rechargeable lithium batteries. *Chem. Mater.* 23, 2027–2029. doi:10.1021/cm200441h

Inada, R., Ishida, K., Tojo, M., Okada, T., Tojo, T., and Sakurai, Y. (2015). Properties of aerosol deposited NASICON-type Li<sub>1.5</sub>Al<sub>0.5</sub>Ge<sub>1.5</sub>(PO<sub>4</sub>)<sub>3</sub> solid electrolyte thin films. *Ceramics Int.* 41, 11136–11142. doi:10.1016/j.ceramint.2015.05.062

and characterization during his visiting in their laboratory on March 2015. This work was partly supported by JSPS KAKENHI [Challenging Exploratory Research and Scientific Research (C)] grant numbers 26630111 and 16K06218 from the Japan Society for the Promotion of Science (JSPS), Research Foundation for the Electrotechnology of Chubu (R-25209) and TOYOAKI Scholarship Foundation.

Inada, R., Kusakabe, K., Tanaka, T., Kudo, S., and Sakurai, Y. (2014a). Synthesis and properties of Al-free Li<sub>7-x</sub>La<sub>3</sub>Zr<sub>2-x</sub>Ta<sub>x</sub>O<sub>12</sub> garnet related oxides. *Solid State Ionics*. 262, 568–572. doi:10.1016/j.ssi.2013.09.008

Inada, R., Shibukawa, K., Masada, C., Nakanishi, Y., and Sakurai, Y. (2014b). Characterization of as-deposited Li<sub>4</sub>Ti<sub>5</sub>O<sub>12</sub> thin film electrode prepared by aerosol deposition method. *J. Power Sources* 244, 646–651. doi:10.1016/j.jpowsour.2013.12.084

Iwasaki, S., Hamanaka, T., Yamakawa, T., West, W. C., Yamamoto, K., Motoyama, M., et al. (2014). Preparation of thick-film LiNi<sub>1/3</sub>Co<sub>1/3</sub>Mn<sub>1/3</sub>O<sub>2</sub> electrodes by aerosol deposition and its application to all-solid-state batteries. *J. Power Sources* 272, 1086–1090. doi:10.1016/j.jpowsour.2014.09.038

Jalem, R., Rushton, M. J. D., Manalastas, W. Jr., Nakayama, M., Kasuga, T., Kilner, J. A., et al. (2015). Effects of Gallium doping in garnet-type Li<sub>7</sub>La<sub>3</sub>Zr<sub>2</sub>O<sub>12</sub> solid electrolytes. *Chem. Mater.* 27, 2821–2831. doi:10.1021/cm5045122

Jin, Y., and McGinn, P. J. (2011). Al-doped Li<sub>7</sub>La<sub>3</sub>Zr<sub>2</sub>O<sub>12</sub> synthesized by a polymerized complex method. *J. Power Sources* 196, 8683–8687. doi:10.1016/j.jpowsour.2011.05.065

Kato, T., Iwasaki, S., Ishii, Y., Motoyama, N., West, W. C., Yamamoto, Y., et al. (2016). Preparation of thick-film electrode-solid electrolyte composites on Li<sub>7</sub>La<sub>3</sub>Zr<sub>2</sub>O<sub>12</sub> and their electrochemical properties. *J. Power Sources* 303, 65–72. doi:10.1016/j.jpowsour.2015.10.101

Kihira, Y., Ohta, S., Imagawa, H., and Asaoka, T. (2013). Effect of simultaneous substitution of alkali earth metals and Nb in Li<sub>7</sub>La<sub>3</sub>Zr<sub>2</sub>O<sub>12</sub> on lithium-ion conductivity. *ECS Electrochem. Lett.* 2, A56–A59. doi:10.1149/2.001307eel

Kim, I., Park, J., Nam, T.-H., Kim, K.-W., Ahn, J.-H., Park, D.-S., et al. (2013). Electrochemical properties of an as-deposited LiFePO<sub>4</sub> thin film electrode prepared by aerosol deposition. *J. Power Sources* 243, 181–186. doi:10.1016/j.jpowsour.2012.12.108

Knauth, P. (2009). Inorganic solid Li ion conductors: an overview. *Solid State Ionics*. 180, 911–916. doi:10.1016/j.ssi.2009.03.022

Kotobuki, M., Kanamura, K., Sato, Y., and Yoshida, T. (2011). Fabrication of all-solid-state lithium battery with lithium metal anode using Al<sub>2</sub>O<sub>3</sub>-added Li<sub>7</sub>La<sub>3</sub>Zr<sub>2</sub>O<sub>12</sub> solid electrolyte. *J. Power Sources* 196, 7750–7754. doi:10.1016/j.jpowsour.2011.04.047

Kumazaki, S., Iriyama, Y., Kim, K.-H., Murugan, R., Tanabe, K., Yamamoto, K., et al. (2011). High lithium ion conductive Li<sub>7</sub>La<sub>3</sub>Zr<sub>2</sub>O<sub>12</sub> by inclusion of both Al and Si. *Electrochem. Commun.* 13, 509–512. doi:10.1016/j.elecom.2011.02.035

Li, Y., Han, J.-T., Wang, C.-A., Vogel, S. C., Xie, H., Xu, M., et al. (2012a). Ionic distribution and conductivity in lithium garnet Li<sub>7</sub>La<sub>3</sub>Zr<sub>2</sub>O<sub>12</sub>. *J. Power Sources* 209, 278–281. doi:10.1016/j.jpowsour.2012.02.100

Li, Y., Han, J.-T., Wang, C.-A., Xie, H., and Goodenough, J. B. (2012b). Optimizing Li<sup>+</sup> conductivity in a garnet framework. *J. Mater. Chem.* 22, 15357–15361. doi:10.1039/C2JM31413D

Li, Y., Wang, Z., Cao, Y., Du, F., Chen, C., Cui, Z., et al. (2015). W-doped Li<sub>7</sub>La<sub>3</sub>Zr<sub>2</sub>O<sub>12</sub> ceramic electrolytes for solid state Li-ion batteries. *Electrochim. Acta* 180, 37–42. doi:10.1016/j.electacta.2015.08.046

Logéat, A., Köhler, T., Eisele, U., Stiaszny, B., Harzer, A., Tovar, M., et al. (2012). From order to disorder: the structure of lithium-conducting garnets Li<sub>7-x</sub>La<sub>3</sub>Ta<sub>x</sub>Zr<sub>2-x</sub>O<sub>12</sub> (x = 0–2). *Solid State Ionics*. 206, 33–38. doi:10.1016/j.ssi.2011.10.023

Murugan, R., Thangadurai, V., and Weppner, W. (2007a). Fast lithium ion conduction in garnet-type Li<sub>7</sub>La<sub>3</sub>Zr<sub>2</sub>O<sub>12</sub>. *Angew. Chem. Int. Ed.* 46, 7778–7781. doi:10.1002/anie.200701144

Murugan, R., Weppner, W., Schmid-Beurmann, P., and Thangadurai, V. (2007b). Structure and lithium ion conductivity of bismuth containing lithium garnets Li<sub>3</sub>La<sub>3</sub>Bi<sub>2</sub>O<sub>12</sub> and Li<sub>6</sub>SrLa<sub>2</sub>Bi<sub>2</sub>O<sub>12</sub>. *Mater. Sci. Eng. B* 143, 14–20. doi:10.1016/j.mseb.2007.07.009

Nemori, H., Matsuda, Y., Mitsuoaka, S., Matsui, M., Yamamoto, O., Takeda, Y., et al. (2015). Stability of garnet-type solid electrolyte Li<sub>k</sub>La<sub>3</sub>A<sub>2-x</sub>B<sub>y</sub>O<sub>12</sub> (A = Nb or Ta, B = Sc or Zr). *Solid State Ionics*. 282, 7–12. doi:10.1016/j.ssi.2015.09.015

- Ohta, S., Kobayashi, T., and Asaoka, T. (2011). High lithium ionic conductivity in the garnet-type oxide  $\text{Li}_{7-x}\text{La}_3(\text{Zr}_{2-x}\text{Nb}_x)\text{O}_{12}$  ( $X = 0-2$ ). *J. Power Sources* 196, 3342–3345. doi:10.1016/j.jpowsour.2010.11.089
- Ohta, S., Komagata, S., Seki, J., and Asaoka, T. (2012). Electrochemical performance of an all-solid-state lithium ion battery with garnet-type oxide electrolyte. *J. Power Sources* 202, 332–335. doi:10.1016/j.jpowsour.2011.10.064
- Ohta, S., Komagata, S., Seki, J., Saeki, T., Morishita, S., and Asaoka, T. (2013). All-solid-state lithium ion battery using garnet-type oxide and  $\text{Li}_3\text{BO}_3$  solid electrolytes fabricated by screen-printing. *J. Power Sources* 238, 53–56. doi:10.1016/j.jpowsour.2013.02.073
- Ohta, S., Seki, J., Yagi, Y., Kihira, Y., Tani, T., and Asaoka, T. (2014). Co-sinterable lithium garnet-type oxide electrolyte with cathode for all-solid-state lithium ion battery. *J. Power Sources* 265, 40–44. doi:10.1016/j.jpowsour.2014.04.065
- Popovici, D., Nagai, H., Fujisima, S., and Akedo, J. (2011). Preparation of lithium aluminum titanium phosphate electrolytes thick films by aerosol deposition method. *J. Am. Ceramic Soc.* 94, 3847–3850. doi:10.1111/j.1551-2916.2011.04551.x
- Rangasamy, E., Wolfenstine, J., and Sakamoto, J. (2012). The role of Al and Li concentration on the formation of cubic garnet solid electrolyte of nominal composition  $\text{Li}_7\text{La}_3\text{Zr}_2\text{O}_{12}$ . *Solid State Ionics*. 206, 28–32. doi:10.1016/j.ssi.2011.10.022
- Ren, Y., Chen, K., Chen, R., Liu, T., Zhang, Y., and Nan, C.-W. (2015a). Oxide electrolytes for lithium batteries. *J. Am. Ceramic Soc.* 98, 3603–3623. doi:10.1111/jace.13844
- Ren, Y., Deng, H., Chen, R., Shen, Y., Lin, Y., and Nan, C.-W. (2015b). Effects of Li source on microstructure and ionic conductivity of Al-contained  $\text{Li}_{6.75}\text{La}_3\text{Zr}_{1.75}\text{Ta}_{0.25}\text{O}_{12}$  ceramics. *J. Eur. Ceramic Soc.* 35, 561–572. doi:10.1016/j.jeurceramsoc.2014.09.007
- Scrosati, B., and Garche, J. (2010). Lithium batteries: status, prospects and future. *J. Power Sources* 195, 2419–2430. doi:10.1016/j.jpowsour.2009.11.048
- Shinawi, H. E., and Janek, J. (2013). Stabilization of cubic lithium-stuffed garnets of the type “ $\text{Li}_7\text{La}_3\text{Zr}_2\text{O}_{12}$ ” by addition of gallium. *J. Power Sources* 225, 13–19. doi:10.1016/j.jpowsour.2012.09.111
- Takada, K. (2013). Progress and prospective of solid-state lithium batteries. *Acta Mater.* 61, 759–770. doi:10.1016/j.actamat.2012.10.034
- Tarascon, J.-M., and Armand, M. (2001). Issues and challenges facing rechargeable lithium batteries. *Nature* 414, 359–367. doi:10.1038/35104644
- Tatsumisago, M., Nagao, M., and Hayashi, A. (2013). Recent development of sulfide solid electrolytes and interfacial modification for all-solid-state rechargeable lithium batteries. *J. Asian Ceramic Soc.* 1, 117–125. doi:10.1016/j.jascer.2013.03.005
- Thangadurai, V., Narayanan, S., and Pinzaru, D. (2014). Garnet-type solid-state fast Li ion conductors for Li batteries: critical review. *Chem. Soc. Rev.* 43, 4714–4727. doi:10.1039/c4cs00020j
- Thangadurai, V., Pinzaru, D., Narayanan, S., and Baral, A. K. (2015). Fast solid-state Li ion conducting garnet-type structure metal oxides for energy storage. *J. Phys. Chem. Lett.* 6, 292–299. doi:10.1021/jz501828v
- Thangadurai, V., and Weppner, W. (2005).  $\text{Li}_6\text{Ala}_2\text{Ta}_2\text{O}_{12}$  (A = Sr, Ba): novel garnet-like oxides for fast lithium ion conduction. *Adv. Funct. Mater.* 15, 107–112. doi:10.1002/adfm.200400044
- Thompson, T., Sharafi, A., Johannes, M. D., Huq, A., Allen, J. L., Wolfenstine, J., et al. (2015). Tale of two sites: on defining the carrier concentration in garnet-based ionic conductors for advanced Li batteries. *Adv. Energy Mater.* 5: 1500096. doi:10.1002/aenm.201500096
- Thompson, T., Wolfenstine, J., Allen, J. L., Johannes, M., Huq, A., Davida, I. N., et al. (2014). Tetragonal vs. cubic phase stability in Al-free Ta doped  $\text{Li}_7\text{La}_3\text{Zr}_2\text{O}_{12}$  (LLZO). *J. Mater. Chem. A* 2, 13431–13436. doi:10.1039/c4ta02099e
- Tong, X., Thangadurai, V., and Wachslan, E. D. (2015). Highly conductive Li garnets by a multielement doping strategy. *Inorg. Chem.* 54, 3600–3607. doi:10.1021/acs.inorgchem.5b00184
- Wang, Y., and Wei, L. (2012). High ionic conductivity lithium garnet oxides of  $\text{Li}_{7-x}\text{La}_3\text{Zr}_{2-x}\text{Ta}_x\text{O}_{12}$  compositions. *Electrochem. Solid State Lett.* 15, A68–A71. doi:10.1149/2.024205esl
- Wolfenstine, J., Ratchford, J., Rangasamy, E., Sakamoto, J., and Allen, J. L. (2012). Synthesis and high Li-ion conductivity of Ga-stabilized cubic  $\text{Li}_7\text{La}_3\text{Zr}_2\text{O}_{12}$ . *Mater. Chem. Phys.* 134, 571–575. doi:10.1016/j.matchemphys.2012.03.054
- Xie, H., Park, K.-S., Song, J., and Goodenough, J. B. (2012). Reversible lithium insertion in the garnet framework of  $\text{Li}_3\text{Nd}_3\text{W}_2\text{O}_{12}$ . *Electrochem. commun.* 19, 135–137. doi:10.1016/j.elecom.2012.03.014

**Conflict of Interest Statement:** The authors declare that the research was conducted in the absence of any commercial or financial relationships that could be construed as a potential conflict of interest.

Copyright © 2016 Inada, Yasuda, Tojo, Tsuritani, Tojo and Sakurai. This is an open-access article distributed under the terms of the Creative Commons Attribution License (CC BY). The use, distribution or reproduction in other forums is permitted, provided the original author(s) or licensor are credited and that the original publication in this journal is cited, in accordance with accepted academic practice. No use, distribution or reproduction is permitted which does not comply with these terms.